Research Article Vol. 33, No. 20 / 6 Oct 2025 / Optics Express 42909
Optics EXPRESS

# Cone-beam X-ray luminescence computed tomography via Laplacian scale mixture prior-driven variational Bayesian method

YITING HE,[1] BIANBIAN YANG,[1] NANNAN CAI,[1] YI CHEN,[1,2,4] YIFAN WANG,[1] HUANGJIAN YI,[1] XINGXING HAO,[1,5] CHENGYI GAO,[3] AND XIN CAO[1,6]

[1]School of Information Science and Technology, Northwest University, Xi'an, Shaanxi 710127, China
[2]School of Electrical and Mechanical Engineering, The University of Adelaide, Adelaide, SA 5005, Australia
[3]Department of Oncology, The First Affiliated Hospital, Xi'an Jiaotong University, Xi'an, Shaanxi 710061, China
[4]yichen.cgz@gmail.com
[5]xingxing.hao@nwu.edu.cn
[6]caoxin918@hotmail.com

**Abstract:** Cone-beam X-ray luminescence computed tomography (CB-XLCT), as an emerging optical molecular imaging modality, has garnered extensive attention due to its capability to monitor the dynamic changes in early-stage tumors. However, the reconstruction of CB-XLCT has been impeded by the low absorption and pronounced scattering properties inherent in biological tissues. Here, a variational Bayesian method based on the Laplacian scale mixture prior has been proposed for the modeling and recovery of sparse signals for CB-XLCT. Within this framework, the scale variable is governed by an inverse gamma distribution, which is employed as the conjugate prior to the Laplacian, thereby enabling an adaptive representation of sparsity levels and enhancing model flexibility. The Laplace approximation has been utilized to derive an analytical form of the posterior distribution, converting the intractable posterior into a Gaussian distribution. Under this approximation, the maximum a posteriori (MAP) estimate has been shown to correspond to the expected value. Additionally, signal recovery has been conducted within the variational Bayesian structure using the expectation-maximization (EM) algorithm, resulting in substantial improvements in reconstruction accuracy. The performance of our method has been assessed through numerical simulations and implantation experiments. Results have demonstrated superior performance in both source localization and morphological restoration, thereby highlighting its potential for advancing CB-XLCT toward preclinical and clinical applications.



## 1. Introduction

X-ray luminescence computed tomography (XLCT) is a hybrid imaging technique that combines the high spatial resolution of X-ray imaging with the high molecular sensitivity of optical imaging. It has demonstrated significant potential for applications in biomedical fields, such as tumor imaging and precision therapy [1]. In this approach, fluorescent nanoprobes are excited by external X-rays, causing them to emit visible light or near-infrared (NIR) signals, which are capable of penetrating tissues and are detected with high sensitivity using charge-coupled devices (CCDs), photomultiplier tubes (PMT), scientific complementary metal-oxide-semiconductor (sCMOS) cameras, and other photosensitive technologies [2]. Compared to other optical molecular imaging techniques [3,4], XLCT leverages the strong penetrating ability of X-rays, allowing for the imaging of targeted fluorescent probes within deep tissues. XLCT systems can be classified

#572142 https://doi.org/10.1364/OE.572142
Journal © 2025 Received 1 Jul 2025; revised 22 Sep 2025; accepted 22 Sep 2025; published 30 Sep 2025

Optics EXPRESS

into narrow beam or pencil beam (NB-XLCT/PB-XLCT) [5] and cone beam (CB-XLCT) [6], depending on the structure of the X-ray excitation beam. NB-XLCT and PB-XLCT generally utilize point-by-point scanning, which provides high resolution but requires extended acquisition times, thus limiting their clinical applicability [7]. In contrast, CB-XLCT employs a cone beam to excite the entire imaging region simultaneously, substantially improving data acquisition efficiency and X-ray dose utilization and making it more suitable for fast, high-throughput imaging applications [8]. Consequently, the CB-XLCT system is adopted in this study to optimize imaging efficiency, thereby making it more suitable for fast, high-throughput imaging applications relevant to practical screening or monitoring. However, due to the low photon absorption and high scattering properties of biological tissues, the image reconstruction problem in CB-XLCT is inherently ill-conditioned [9].

To address the ill-conditioning inherent in CB-XLCT, various improvement strategies have been developed. Sparsity that is acknowledged as a robust prior is employed to enforce structural constraints on the solutions. As a result, its application has become widespread in the resolution of inverse problems [10]. Sparse regularization approaches were initially developed by Chen et al. [11,12]. In their work, an incomplete variable truncation conjugate gradient (IVTCG) algorithm was integrated with a permissible region strategy (PRS), leading to a notable enhancement in reconstruction performance. In order to integrate the advantages of various regularization forms, methods such as manifold regularization, elastic net ($L_1$-$L_2$) regularization, and sparse non-convex $L_p$ regularization have been developed successively [13–15]. Furthermore, both internal and external iterative reconstruction methods with restart strategies, along with permissible region (PR) strategies, have been further explored [16,17], aiming to reset the permissible region and accelerate the convergence of outer iterations. Recently, Liu et al. investigated adaptive reconstruction algorithms based on the maximum likelihood expectation maximization framework (ADFISTA-MLEM) [18], which further improved reconstruction accuracy and convergence stability.

While regularization methods have demonstrated strong performance in computational efficiency and reconstruction accuracy, they exhibit limitations in edge preservation, often leading to image blurring and the enhancement of artifacts [14]. To address this issue, Singh et al. introduced a dictionary learning framework [19], where adaptive learning of dictionary elements and sparse representation were employed to preserve the original structural details of tumor regions. Methods such as dictionary learning and group structure (DLGS) [20] and compressed sensing collaborative dictionary learning [21] have effectively captured sparse features, resulting in stable and accurate reconstructions. However, this approach is highly dependent on dictionary selection and the learning process, which may lead to high computational complexity and increased susceptibility to noise [20]. Therefore, a reconstruction strategy must be developed to preserve structural details and enhance robustness while simultaneously incorporating prior knowledge and enabling effective uncertainty modeling.

The shortcomings of the methods above have been addressed by employing a Bayesian framework [22], in which probabilistic modeling is combined with prior knowledge to alleviate the ill-conditioned nature of the CB-XLCT reconstruction process substantially. Specifically, the complex optimization problem is reformulated as posterior probability inference, enabling systematic integration of prior information and observed data, which effectively suppresses noise interference. Reconstruction accuracy is thereby improved, and image features are more accurately delineated. For example, hierarchical Bayesian and naive Bayesian techniques [23,24] have been shown to significantly reduce computational complexity through multi-level iterative algorithms, while sparse Bayesian methods [25] further enhance the capability to recover sparse signals. Concurrently, variational Bayesian and Bayesian optimization methods [26,27] have seen continuous development within the medical imaging domain, utilizing variational inference and hierarchical modeling to effectively manage high-dimensional sparse challenges, thereby

Optics EXPRESS

improving the accuracy of source localization and morphological reconstruction. As a result, the Bayesian framework has provided important perspectives for three-dimensional sparse reconstruction. Nonetheless, the practical implementation of Bayesian methods remains limited due to their considerable dependence on the selection of prior information.

In this paper, a variational Bayesian method based on the Laplace scale mixture (VB-LSM) prior is proposed for sparse signal reconstruction. In this approach, the advantages of the LSM prior in modeling both sparsity and multi-scale structures are comprehensively leveraged. The scale parameter is formulated as an inverse Gamma distribution, enabling the intrinsic sparse characteristics and hierarchical patterns of the signal to be accurately captured. As a result, the representational capability of the signal is markedly improved. During the inference phase, to address the computational challenges posed by the intractable posterior, a Laplace approximation is adopted to approximate the non-analytic distribution with a Gaussian form, significantly reducing the complexity of inference. Furthermore, maximum a posteriori (MAP) estimates are efficiently obtained using expected values under the current posterior estimates, allowing for accurate parameter inference and uncertainty quantification. To further refine posterior estimation, a variational Bayesian inference framework within the expectation-maximization (EM) scheme is incorporated. This framework enables a more complete characterization of the posterior induced by the LSM prior, improving the ability of the model to recover sparse structures. Overall, the proposed VB-LSM method achieves a favorable balance between representational power and computational efficiency.

The organization of this paper is as follows: Section 2 presents the CB-XLCT forward propagation and the VB-LSM method. Section 3 describes the experimental setup. Section 4 displays the experimental results. Section 5 offers a discussion and conclusion of our work.

## 2. Methodology

### 2.1. Forward propagation

According to Lambert-Beer's law [28], the density distribution of X-rays as they pass through tissue can be expressed as follows:

$$X(r) = X_0 exp\left\{-\int_{r_0}^{r} \mu t(\omega) d\omega\right\} \tag{1}$$

where $X(r)$ is the X-ray intensity at position $r$, $X_0$ is the X-ray concentration at the initial position, and $\mu t(\omega)$ is the X-ray attenuation coefficient at position $\omega$, which can be calculated from the X-ray projection data.

Subsequently, based on the principles of CB-XLCT imaging, nanoparticles within biological tissue are excited by external X-rays, leading to the emission of near-infrared light. This process can be expressed as follows:

$$S(r) = \delta X(r)\rho(r) \tag{2}$$

where $S(r)$ is the light source, $\delta$ is the photon yield, and $\rho(r)$ is the nanoparticle concentration at position $r$.

The transportation process of visible light or NIR light in biological tissue can be modeled by the radiative transfer equation (RTE), but it is challenging to solve RTE directly because of its high mathematical complexity. Due to the highly scattering and weak absorption properties of the visible or NIR spectral window in biological tissue, in general, the RTE model can be simplified to the following steady-state diffusion equation (DE) model [29] with Robin-type boundary condition, which is defined as follows:

$$\begin{cases} -\nabla[D(r)\nabla\Phi(r)] + \mu_a(r)\Phi(r) = S(r), r \in \Omega \\ 2\gamma D(r)[\nu\nabla\Phi(r)] + \Phi(r) = 0, r \in \partial\Omega \end{cases} \tag{3}$$

Optics EXPRESS

where $D(r)$ is the diffusion coefficient, which can be calculated by $D(r) = [3(\mu_a(r) + \mu_s'(r))]^{-1}$, and $\mu_a(r)$ and $\mu_s'(r)$ are the absorption and reduced scattering coefficients at the position $r$, $\Phi(r)$ is the photon flux density, $\Omega$ denotes the domain occupied by the imaging object, $\gamma$ represents the boundary mismatch factor, and $\nu$ is the outward unit normal vector on the boundary $\partial\Omega$.

Ultimately, the diffusion equation is numerically approximated by means of the finite element method [30]. Accordingly, Eq. (3) is reformulated as the following linear expression:

$$\Phi = Ax \tag{4}$$

where $\Phi$ represents the measurable infrared light data on the surface of the biological tissue, $A$ is an $m \times n$ sparse matrix, and $x$ is the distribution of internal fluorescent source.

### 2.2. Reconstruction based on VB-LSM method

The primary aim of CB-XLCT is to reconstruct the unknown spatial distribution of nanoparticle-based fluorescent agents $x$, based on measurement data $\Phi$ collected in the visible or near-infrared spectrum. However, due to the inherently low absorption and strong scattering characteristics of biological tissues, the system matrix $A$ is rendered severely ill-conditioned. As a result, the inverse problem becomes highly ill-conditioned. To overcome this challenge, Eq. (4) has been reformulated as a minimization objective function based on the principles of compressed sensing. Through this transformation, the acquisition of sparser and more robust solutions is facilitated.

$$\hat{x} = \underset{x}{arg\ min}\ ||\Phi - Ax||_2^2 \tag{5}$$

where $||\cdot||_k$ is the $k$ -norm operator, $\tau$ is the sparse constraint coefficient that regulates the degree of signal sparsity. However, due to the non-convex nature of the objective function, direct optimization proves to be challenging. Therefore, in CB-XLCT image reconstruction, the posterior distribution is approximated through the integration of the expectation-maximization (EM) framework and the variational Bayesian (VB) method.

In addition, during the CB-XLCT imaging procedure, the effect of measurement noise must be considered. The noise term $\eta$ is assumed to follow an additive Gaussian white noise model characterized by zero mean and variance of $\beta^{-1}$. The corresponding probability distribution is expressed as:

$$p(\eta) = \mathcal{N}(\eta|0, \beta^{-1}I) \tag{6}$$

where $I \in \mathbb{R}^{N\times N}$ is the identity matrix.

At the same time, the noise precision $\beta$, defined as the reciprocal of the noise variance, is constrained to be strictly positive. Consequently, its prior distribution must be defined on the positive real domain. The Gamma distribution [31] is commonly adopted due to its support of positive values and the flexibility provided by its shape and scale parameters, which facilitate the encoding of various prior beliefs. Furthermore, within the framework of variational Bayesian inference, the Gamma distribution is employed as a conjugate prior for the precision parameter in Gaussian noise models, thereby significantly simplifying the computation of the posterior distribution. The explicit form is expressed as follows:

$$p(\beta; a, b) = \mathcal{G}(\beta; a, b) = \frac{b^a}{\Gamma(a)}\beta^{a-1}exp(-b\beta) \tag{7}$$

where $\Gamma(a)$ is the Gamma function, and the scaling parameters $a$ and $b$ are set to $10^{-4}$ [32], ensuring that the prior for $\beta$ is non-informative.

Based on the previously described measurement framework and noise assumptions, and within the context of Bayesian theory, the conditional probability of the fluorescence distribution $x$,

Optics EXPRESS

noise precision $\beta$, and observed data $\Phi$ is represented by a Gaussian distribution.

$$p(\Phi|x,\beta) = \mathcal{N}(\Phi|Ax,\beta^{-1}I) = (2\pi)^{-\frac{N}{2}}\beta^{\frac{N}{2}}exp(-\frac{\beta}{2}||\Phi - Ax||^2) \tag{8}$$

Within the Bayesian framework, the variable $x$ is regarded as a random variable, and a sparse prior is imposed to facilitate accurate reconstruction of the nanofluorescence distribution. Gaussian scale mixture (GSM) priors have been widely adopted in conventional methods [33]. However, to characterize the multiscale and sparse properties of the signal more effectively, this study employs a Laplacian scale mixture (LSM) prior [34].

The local heterogeneity of the sparse coefficients is captured by employing a collection of non-stationary Laplace distributions, each defined by a unique scale parameter $\lambda_m (m = 1, \ldots, M)$. The explicit formulation is provided as follows:

$$p(x|\lambda) = \prod_{m=1}^{M} \mathcal{L}(x_m|0,\lambda_m) = \prod_{m=1}^{M} \frac{1}{2\lambda_m} exp\left(-\frac{|x_m|}{\lambda_m}\right) \tag{9}$$

where $\mathcal{L}(x_m|0,\lambda_m)$ is the Laplace distribution with scale parameter $\lambda_m$, modeling each sparse coefficient $x_m$.

The scale parameter $\lambda_m$ is modeled using an inverse Gamma distribution as a prior, thereby improving the flexibility and adaptability of the model.

$$p(\lambda;c,d) = \prod_{m=1}^{M} \mathcal{IG}(\lambda_m;c,d) = \prod_{m=1}^{M} \frac{d^c}{\Gamma(c)} \lambda_m^{-c-1} exp\left(-\frac{d}{\lambda_m}\right) \tag{10}$$

where $\Gamma(c)$ is the Gamma function, $c$ is the shape parameter, and $d$ is the scale parameter of the Gamma distribution. To ensure a highly non-informative prior, both $c$ and $d$ are set to $10^{-4}$ [32], where this choice mitigates the influence of excessive prior knowledge.

The prior distributions of the Laplace and inverse gamma are combined to derive the marginal likelihood of the sparse signal $x$. By eliminating the scaling parameter $\lambda_m$, the expression for the marginal likelihood is obtained as follows:

$$\begin{aligned} p(w;c,d) &= \prod_{m=1}^{M} p(w_m;c,d) \\ &= \prod_{m=1}^{M} \int_0^{+\infty} p(w_m|\lambda_m)p(\lambda_m;c,d)d\lambda_m \\ &= \prod_{m=1}^{M} \frac{cd^c}{2(|w_m| + d)^{c+1}} \end{aligned} \tag{11}$$

In the practical implementation of sparse signal recovery, the posterior distribution is estimated by employing a VB inference method grounded in the EM algorithm [35]. Specifically, during each iteration, the VB technique is applied in the E-step to approximate the posterior distribution, thereby enabling the computation of the expected values of latent variables. Subsequently, model parameters are updated in the M-step based on these expectations. To further improve the precision of posterior estimation, the Laplace approximation [36] is incorporated to enhance the representational capacity of the variational distribution. This approach has been shown to effectively capture sparse structures in XLCT image reconstruction while significantly diminishing reconstruction errors and elevating the overall image fidelity.

Specifically, the sparse signal $x$ is recovered through maximum a posteriori (MAP) estimation, which is performed by maximizing the posterior distribution $p(x|\Phi,\lambda,\beta)$ within the framework of the EM algorithm. The procedure is formally expressed as follows:

$$\hat{x}_{MAP} = \underset{x}{arg\,max}\, p(x|\Phi,\lambda,\beta) \tag{12}$$

The EM algorithm is an iterative method employed for optimizing parameter estimation. It comprises two primary steps: the expectation step (E-step) and the maximization step (M-step).

Optics EXPRESS

In the E-step, the expectation of the log-likelihood function is calculated. The primary task of this step is to determine the posterior distribution of the latent variables. In the VB-LSM method, it is assumed that the posterior distribution of the signal $x$ is conditionally independent, i.e., $p(x|\Phi) = p(x|\lambda, \beta)p(\lambda)p(\beta)$. The $Q$-function, which represents the expected log-likelihood given the current parameter estimates, is derived by evaluating the expectation function. The goal of the E-step is to compute the expectation with respect to the latent variables, which is formally expressed as:

$$\begin{aligned} Q(x; \hat{x}^{(t)}) &= E_{\lambda,\beta|\Phi,\hat{x}^{(t)}}[logp(x|\Phi, \lambda, \beta)] \\ &= E_{\lambda,\beta|\Phi,\hat{x}^{(t)}}[log\ p(\Phi|x, \beta) + log\ p(x|\lambda)] \end{aligned} \tag{13}$$

where $E_{\lambda,\beta|\Phi,\hat{x}^{(t)}}$ is the expected value of $p(\lambda, \beta|\Phi, \hat{x}^{(t)})$, $\hat{x}^{(t)}$ is the sparse signal estimated at the $t$-th iteration.

In the M-step, the signal estimate is updated by maximizing the $Q$-function. Maximizing the $Q$-function represents a critical step in the EM algorithm. This process results in the updated signal estimate $\hat{x}^{(t+1)}$. The goal of the M-step is to determine a new signal estimate that maximizes the $Q$-function. The updated formula is provided as follows:

$$\hat{x}^{(t+1)} = arg\ \underset{x}{max}[Q(x; \hat{x}^{(t)})] \tag{14}$$

The signal recovery accuracy is enhanced through the optimization of the $Q$-function. By iterating multiple times, the EM algorithm effectively determines the optimal estimate of the signal.

The core of the EM algorithm is based on the computation of the $Q$-function, which requires the derivation of the posterior distribution of the latent variables. In the VB-LSM algorithm, variational Bayesian inference is utilized to approximate the posterior distribution. Specifically, the posterior values of all latent variables are derived within the Bayesian inference framework:

$$p(x, \lambda, \beta|\Phi) = \frac{P(\Phi|x, \beta)p(x|\lambda)p(\beta)p(\lambda)}{p(\Phi)} \tag{15}$$

where $p(x, \lambda, \beta|\Phi)$ is the posterior distribution, $p(x|\lambda)$ is the prior distribution, $P(\Phi|x, \beta)$ is the likelihood function, representing the probability of observing the data $\Phi$ given the latent variable $x$ and the noise parameter $\beta$, $p(\beta)$ is the prior distribution of the hyperparameter $\beta$, $p(\lambda)$ is the prior distribution of the hyperparameter $\lambda$, and $p(\Phi)$ is the marginal likelihood of the observed data.

Therefore, the latent variables are consolidated into a unified probability density function:

$$p(\Phi) = \iiint p(\Phi|x, \beta)p(x|\lambda)p(\beta)p(\lambda)dxd\lambda d\beta \tag{16}$$

To simplify the intractable integral computations, approximate Bayesian inference is employed. The associated posterior distributions are assumed to be factorized and statistically independent. The corresponding formulation is presented as follows:

$$p(x, \lambda, \beta|\Phi) \approx q(x, \lambda, \beta) = q(x)q(\lambda)q(\beta) \tag{17}$$

Within the EM framework, the logarithmic form of the variational distribution $q(x)$ associated with the signal $x$ is formulated as follows:

$$\begin{aligned} log\ q(x) &= \langle log\ p(\Phi, x, \lambda, \beta)\rangle_{q(\lambda)q(\beta)} \\ &= \langle log\ p(\Phi|x, \beta)\ p(x|\lambda)\rangle_{q(\lambda)q(\beta)} \end{aligned} \tag{18}$$

where $\langle\cdot\rangle_{q(\lambda)q(\beta)}$ represents the expected value with respect to the probability density functions $q(\lambda)$ and $q(\beta)$. For simplicity, $\langle\cdot\rangle_{q(\lambda)q(\beta)}$ will be denoted as $\langle\cdot\rangle$ in the subsequent descriptions.

Optics EXPRESS

Owing to the non-conjugacy between the Laplace prior in Eq. (10) and the Gaussian likelihood in Eq. (9), the analytical derivation of the posterior distribution $q(x)$ is rendered challenging. To overcome this difficulty, the Laplace approximation is applied. A second-order Taylor expansion is conducted around the MAP estimate $\hat{x}_{MAP}$ to approximate the posterior distribution effectively. The corresponding objective function for the Laplace approximation is given as follows:

$$\begin{aligned} L(x) &= -\langle log p(\Phi|x,\beta)\rangle \\ &= \frac{\langle\beta\rangle}{2}||\Phi - Ax||^2 + \sum_{m=1}^{M}\left\langle\frac{1}{\lambda_m}\right\rangle|x_m| \end{aligned} \tag{19}$$

where $p(\Phi|x,\lambda,\beta) \propto p(\Phi|x,\beta)p(x|\lambda)$, the MAP estimation can be calculated by $\hat{x}_{MAP} = \arg\min_X\{L(x)\}$.

The gradient and Hessian matrix corresponding to $L(x)$ can be derived for optimization through the application of the aforementioned Laplace approximation. In the MAP estimation, by setting $\nabla_x L(x) = 0$, the following is obtained:

$$\nabla_x L(x) = (\langle\beta\rangle A^T A + \Lambda)^{-1} A^T \Phi \tag{20}$$

where $\Lambda = \text{diag}\left[\left\langle\frac{1}{\lambda_m}\right\rangle \frac{1}{|w_m|}\right]$ denotes a diagonal matrix that contains prior information related to the signal.

The estimate $\hat{x}_{MAP}$ is derived based on Eq. (20).

$$\hat{x}_{MAP} = \langle\beta\rangle\,(\langle\beta\rangle A^T A + \Lambda)^{-1} A^T \Phi \tag{21}$$

Building upon this, the Laplace approximation is subsequently introduced. The distribution $q(x)$ is approximated by a second-order Taylor expansion, as presented below:

$$log\ q(x) \approx log\ q(\hat{x}_{MAP}) + \frac{1}{2}(x-\hat{x}_{MAP})^T H(\hat{x}_{MAP})(x-\hat{x}_{MAP}) \tag{22}$$

Equation (22) represents the second-order Taylor expansion of $q(x)$ around the MAP estimate $x$. The first-order term $(x-\hat{x}_{MAP})^T \nabla_x log\ q(x)|_{x=\hat{x}_{MAP}}$ is null. $H(\hat{x}_{MAP})$ denotes the value of the Hessian matrix of $log\ q(x)$ evaluated at $\hat{x}_{MAP}$. The derivation is presented below:

$$H(\hat{x}_{MAP}) = \nabla_x^2 log q(x)|_{x=\hat{x}_{MAP}} = -\nabla_x^2 L(x)|_{x=\hat{x}_{MAP}} \tag{23}$$

The term $\nabla_x^2 L(x) \approx \langle\beta\rangle\,\mathrm{A}^T\mathrm{A} + \Lambda$ is derived from Eq. (20), $\Lambda$ is treated as independent of $x$. Consequently, the posterior distribution $q(x)$ is approximated as a Gaussian distribution, with its precision matrix denoted by $\sum$. The equation is expressed as follows:

$$q(x) \approx \frac{1}{C} exp\{-\frac{1}{2}(x-\hat{x}_{MAP})^T \cdot \sum^{-1}(x-\hat{x}_{MAP})\} \tag{24}$$

where $\sum = (\langle\beta\rangle\,\mathrm{A}^T\mathrm{A} + \Lambda)^{-1}$, or equivalently $\sum = \wedge^{-1} - \wedge^{-1}\mathrm{A}^T(\langle\beta\rangle^{-1} I + \mathrm{A}\wedge^{-1}\mathrm{A}^T)^{-1}\mathrm{A}\wedge^{-1}$, is expressed using the Woodbury matrix identity. In this equation, $C$ represents a normalization constant, given by $C = \int_{-\infty}^{+\infty} \exp\{-1/2(x-\hat{x}_{MAP})^T \cdot \sum^{-1}(x-\hat{x}_{MAP})\}dx$.

Optics EXPRESS

Consequently, the posterior distribution $q(x)$ of the sparse signal is further simplified as:

$$q(x) \approx \mathcal{N}(x|\mu, \sum) \tag{25}$$

in which,

$$\mu = \hat{x}_{MAP} = \langle\beta\rangle \sum A^T \Phi \tag{26}$$

Similar to Eq. (18), the posterior distribution of $q(\lambda)$ can be derived. The logarithmic form of $q(\lambda)$ is expressed as:

$$\begin{aligned} log\ q(\lambda) &= \langle logp(x, \Phi, \lambda, \beta)\rangle_{q(x)q(\beta)} \\ &= \langle log\ p(x|\lambda)p(\lambda))\rangle_{q(x)q(\beta)} \\ &= -\sum_{m=1}^{M} log\ \lambda_m - \sum_{m=1}^{M} \frac{\langle|x_m|\rangle}{\lambda_m} - (c+1)\sum_{m=1}^{M} log\ \lambda_m - d\sum_{m=1}^{M} \frac{1}{\lambda_m} \\ &= [-(c+1)-1]\sum_{m=1}^{M} log\ \lambda_m - \sum_{m=1}^{M} (d + \langle|x_m|\rangle)\frac{1}{\lambda_m} \end{aligned} \tag{27}$$

As can be observed from Eq. (27), $q(\lambda)$ is also an inverse Gamma distribution. Therefore, it can be expressed as:

$$q(\lambda) = \prod_{m=1}^{M} \mathcal{IG}(\lambda_m|\tilde{c}, \tilde{d}_m) \tag{28}$$

in which,

$$\tilde{c} = c + 1 \tag{29}$$

$$\tilde{d}_m = d + \langle|x_m|\rangle \tag{30}$$

In addition, the posterior distribution of $\beta$, denoted as $q(\beta)$, can be derived as follows:

$$\begin{aligned} logq(\beta) &= \langle logp(w, \Phi, \lambda, \beta)\rangle_{q(w)q(\lambda)} \\ &= \langle logp(\Phi|w, \beta)p(\beta))\rangle_{q(w)q(\lambda)} \\ &= \frac{N}{2} log\beta - \frac{\beta}{2}\left\langle||\Phi - Ax||^2\right\rangle + (a-1)log\beta - b\beta \\ &= \left(a + \frac{N}{2} - 1\right) log\ \beta - \left(\frac{1}{2}\left\langle||\Phi - Ax||^2\right\rangle + b\right)\beta \end{aligned} \tag{31}$$

The probability density function of the Gamma distribution is formulated as follows, and it is utilized to describe the statistical characteristics of the associated random variable:

$$q(\beta) = \mathcal{G}(\beta|\tilde{a}, \tilde{b}) \tag{32}$$

in which,

$$\tilde{a} = a + \frac{N}{2} \tag{33}$$

$$\tilde{b} = b + \frac{1}{2}\left\langle||\Phi - Ax||^2\right\rangle \tag{34}$$

Ultimately, the posteriors presented in Eq. (25), Eq. (28), and Eq. (32) are employed to estimate the sparse signal and latent variables by iteratively updating their expected values until the desired

Optics EXPRESS

estimation accuracy is attained. The expected updates are provided as follows:

$$\langle x\rangle = \mu = \langle\beta\rangle\left(\langle\beta\rangle A^T A + diag\left[\left\langle\frac{1}{\lambda_m}\right\rangle\frac{1}{\langle|x_m|\rangle}\right]\right)^{-1}A^T\Phi \tag{35}$$

$$\left\langle\frac{1}{\lambda_m}\right\rangle = \frac{\tilde{c}}{\tilde{d}_m} = \frac{c+1}{d+\langle|x_m|\rangle} \tag{36}$$

$$\langle\beta\rangle = \frac{\tilde{a}}{\tilde{b}} = \frac{N+2a}{\left\langle||\Phi - Ax||^2\right\rangle + 2b} \tag{37}$$

To compute the update formulas mentioned above, the matrix for $x$ must be derived, encompassing $\langle|x_m|\rangle$ and $\left\langle||\Phi - Ax||^2\right\rangle$ . The corresponding expressions are provided as follows:

$$\begin{aligned}\langle|x_m|\rangle &= \sqrt{\frac{2\Sigma_x^{m,m}}{\pi}}F_1\left[-\frac{1}{2},\frac{1}{2},-\frac{1}{2}\left(\frac{\mu_m^2}{\Sigma_x^{m,m}}\right)\right]\\ &= \sqrt{\frac{2\Sigma_x^{m,m}}{\pi}}\exp\left(-\frac{\mu_m^2}{2\Sigma_x^{m,m}}\right) + |\mu_m| erf\left(\sqrt{\frac{\mu_m^2}{2\Sigma_x^{m,m}}}\right)\end{aligned} \tag{38}$$

$$\left\langle||\Phi - Ax||^2\right\rangle = ||\Phi - Ax||^2 + tr[\Sigma A^T A] \tag{39}$$

where $F_1[a,b,c] = \sum_{n=0}^{+\infty}\frac{a^{(n)}}{b^{(n)}}\frac{z^n}{n!}$ represents the conjugate hypergeometric function of Kummer, and $x^{(n)}$ is the rising factorial, defined as $x^{(n)} \triangleq x(x+1)(x+2)\cdots(x+n+1)$. Additionally, $\mathrm{erf}(x) = 2/\sqrt{\pi}\int_0^x e^{-t^2}dt$ is the error function.

In summary, during each iteration of the algorithm, the sparse signal $x$ is updated in accordance with Eq. (35), incorporating the estimated scaling parameter $\lambda$ and the inverse noise variance $\beta$. Subsequently, the parameters $1/\lambda_m$ and $\beta$ are iteratively refined using Eq. (36) and Eq. (37).

Through iterative alternation of the aforementioned steps, the accuracy and stability of nanophosphor distribution reconstruction are gradually improved. The difficulties associated with the ill-conditioned system matrix and measurement noise in CB-XLCT are effectively mitigated. The parameter updating scheme of the VB-LSM algorithm is thoroughly described in Algorithm 1.

## 3. Experiment design

To assess the performance of the VB-LSM method, both numerical simulations and implantation experiments were performed. The proposed method was benchmarked against Fast-Laplace [25], FISTA [12], IVTCG [18] and SBL-LCGL [25]. All experimental procedures were executed on a personal computer configured with an Intel Core i5-10210U CPU (1.60GHz) and 8GB of RAM.

### 3.1. Evaluation metrics

Localization error (LE), dice coefficient (DICE) and runtime (Time) were utilized as quantitative evaluation metrics [37]. The respective mathematical formulations are provided below.

LE is defined as the Euclidean distance between the actual source center $L_1$ and the estimated source center $L_2$. The value of LE lies within the range of 0 to 1, where values closer to 0 signify enhanced localization precision.

$$LE = ||L_1 - L_2||_2^2 \tag{40}$$

DICE is employed to measure the extent of overlap between the actual target region $R_1$ and the reconstructed region $R_2$. It ranges from 0 to 1, with values approaching 1 indicating improved reconstruction fidelity.

$$DICE = 2\frac{|R_1 \cap R_2|}{|R_1| + |R_2|} \tag{41}$$

Optics EXPRESS

**Algorithm 1. Algorithm 1: VB-LSM**

**Input:** System matrix $A$, surface flux $\Phi$, initial value of sparse signal $x$, hyperparameters $a$, $b$, $c$, $d$, initial value of noise precision $\beta_0 = 1$, scaling parameter $\lambda_1 = 1$.
**Initialization:** Maximum number of iterations $k_{max} = 1000$, error threshold $err = 1e-6$, initial residual vector $r^0 = \Phi - Ax^0$, current iteration number $k = 1$.
**While**
**Step 1:** Update the parameters and expectations of the noise precision $\beta$: Eq. (33), Eq. (34), and Eq. (37).
**Step 2:** Update the parameters and expectations of the scaling parameter $\lambda_m$: equations Eq. (29), Eq. (30), and Eq. (36).
**Step 3:** Compute the expectation of the sparse signal $x$.

$$\langle |x_m| \rangle = \sqrt{\frac{2\Sigma_x^{m,m}}{\pi}} \exp\left(-\frac{\mu_m^2}{2\Sigma_x^{m,m}}\right) + |\mu_m| \mathrm{erf}\left(\sqrt{\frac{\mu_m^2}{2\Sigma_x^{m,m}}}\right)$$

**Step 4:** Update the posterior distribution of the sparse signal $x$.

$$\langle x \rangle = \langle \beta \rangle (\langle \beta \rangle \mathrm{A}^T \mathrm{A} + \mathrm{diag}\,[\langle \frac{1}{\lambda_m} \rangle \frac{1}{\langle |x_m| \rangle}])^{-1} \mathrm{A}^T \Phi$$

**Step 5:** Compute the residual and check the convergence condition.

$$r^k = \Phi - A\langle x \rangle$$

The iteration stops if $r^k < err$ or $k > k_{max}$.
**End While**
**Output:** $x = \langle x \rangle$.

### 3.2. Numerical simulation experiments

In the numerical simulation experiments, a cylindrical model with a radius of 10 mm and a height of 30 mm was designed to simulate biological structures, as shown in Fig. 1(a). The model contains five organs, including muscle, heart, bone, lung, and liver. Moreover, all experiments in this work are based on single spectrum (650 nm). Here, the optical parameters of these organs at 650 nm are consistent with that in Ref. [38], as shown in Table 1. The intensity of each source is 1 nw/mm$^3$, and the fluorescence distribution of the surface was simulated using the molecular optical simulation environment (MOSE) [39] based on the Monte Carlo method, as depicted in Fig. 1(e) and Fig. 1(f). In all simulations, for the inverse reconstruction, the cylinder model was discretized into a uniform tetrahedral mesh, including 4626 nodes and 25840 tetrahedral elements using the COMSOL Multiphysics 6.1 platform (COMSOL, Inc., Burlington, Massachusetts, USA), and the mean element edge size is 1.37 mm, as shown in Fig. 1(b).

**Table 1. Optical parameters of the organs inside the cylindrical model**

| Tissues | $\mu_{ax}(mm^{-1})$ | $\mu_{sx}'(mm^{-1})$ | $\mu_{am}(mm^{-1})$ | $\mu_{sm}'(mm^{-1})$ |
|---|---|---|---|---|
| muscle | 0.075 | 0.412 | 0.047 | 0.312 |
| heart | 0.050 | 0.944 | 0.033 | 0.820 |
| bone | 0.052 | 2.442 | 0.033 | 2.114 |
| lung | 0.168 | 2.157 | 0.105 | 2.048 |
| liver | 0.302 | 0.668 | 0.192 | 0.602 |

The cylindrical model is adopted due to its capacity to simplify the geometric structure of biological systems, thereby improving computational efficiency. This model is particularly appropriate for preliminary molecular optical simulations and for investigating interactions within multi-organ systems. Through this simplification, the model effectively represents the overall functions and interactions of five organs, establishing a solid balance between computational

Optics EXPRESS

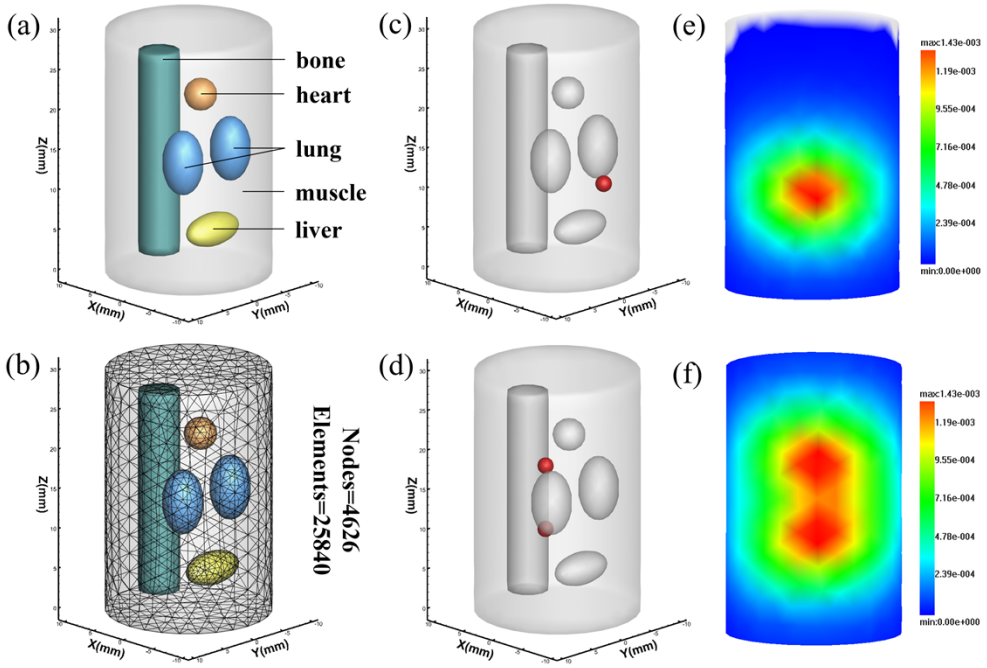


**Fig. 1.** (a) The 3D view of the main organs of cylindrical phantom. (b) The 3D view of meshed biological tissues. (c) Cylindrical phantom with single-target. (d) Cylindrical phantom with dual-target. (e) Forward simulation of cylindrical phantom with single-target. (f) Forward simulation of cylindrical phantom with dual-target.

complexity and simulation accuracy. Despite the simplification of certain details, the model continues to serve as a reliable foundation for subsequent research and is highly suitable for macro-level analysis and validation.

Three experimental setups were designed, including single-source experiment, dual-source experiment, and anti-noise experiment. In the single-source experiment, a sphere with a radius of 1 mm and a center located at (-5, -3, 11) mm was modeled to represent a tumor, as shown in Fig. 1(c). In the dual-source experiment, two spheres, each with a radius of 1 mm, were positioned at centers (-1, 3, 11) mm and (-1, 3, 19) mm, as shown in Fig. 1(d). In the anti-noise experiment, Gaussian noise was introduced at levels of 5%, 10%, 15%, 20%, and 25% to the single-source experiment to evaluate the robustness of the VB-LSM method.

### 3.3. *Implantation experiment*

In the implantation experiment, a flexible plastic tube with a radius of 1 mm was carefully shaped into an approximate sphere and subsequently implanted into the body of an adult BALB/C nude mouse (approximately 6 to 8 weeks of age). The tube was preloaded with approximately 20 $\mu L$ of $Gd_2O_2S$: Tb nanophosphors to simulate a localized target, with a reduced scattering coefficient of $10\,mm^{-1}$. The coordinates of the implant were (11, 14.5, 21) mm, which correspond to the center position in the CT image. All experimental procedures are under the approval of the Animal Ethics Committee of the Northwest University of China, and all procedures were conducted under isoflurane anesthesia to alleviate discomfort.

Imaging system contains a cone-beam X-ray source (Apogee, Oxford Instruments, USA), an electron-multiplying CCD (EMCCD) camera (PIXIS 2048, Princeton Instruments, USA), a CMOS X-ray detector (C7921CA-02, Hamamatsu, Japan), and a rotation platform, as depicted in

Optics EXPRESS

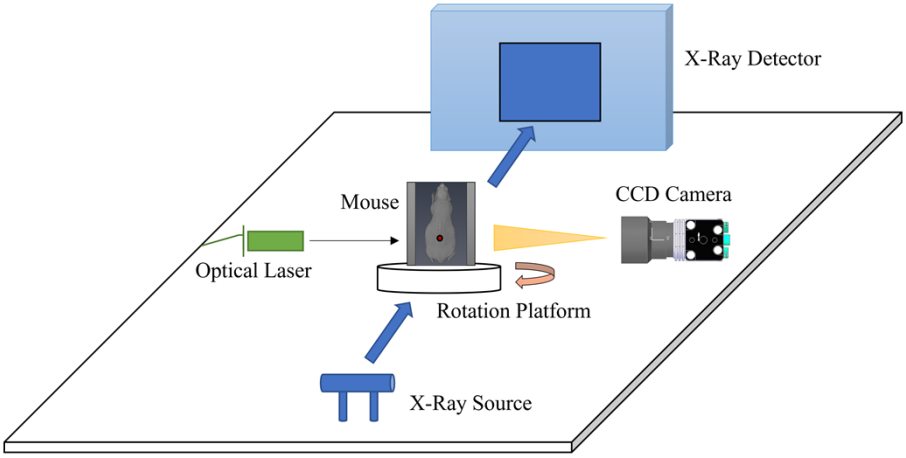


**Fig. 2.** The schematic diagram of the CB-XLCT system.

Fig. 2. During the procedure, the mouse was securely positioned on the rotation platform and rotated through 360° in 1° increments. The X-ray source was operated at 50 KVp and 1 mA to stimulate the internal nanophosphors. High-resolution computed tomography images were acquired using the CMOS X-ray detector, while optical emissions at 620 nm were recorded by the EMCCD sensor. Next, the major organs of the mouse, including the muscle, heart, lung, stomach, liver, and kidney, were segmented using Amira software (Amira, Visage Imaging, Australia). The segmented anatomical structures were subsequently incorporated into an integrated three-dimensional model of the mouse torso. Finally, the 2D fluorescence images obtained from the CB-XLCT system were registered and mapped onto the 3D surface of the mouse using predefined registration points.

## 4. Results

### *4.1. Numerical simulation experiments*

#### 4.1.1. Single-source experiment

The reconstruction results of the single-source experiment are shown in Fig. 3. Quantitative evaluations of the five approaches are additionally provided in Table 2. As illustrated in Fig. 3, the reconstruction achieved by the VB-LSM method is closer to the actual light source than that obtained with the other four techniques. The LE is 0.277 mm, corresponding to a 48.6% decrease relative to the next-best IVTCG scheme. A DICE of 0.857 is attained, signifying considerable overlap in the light-source region, while the computational time remains slightly higher than the average. In summary, the spatial structure of the true light source is effectively reconstructed by the VB-LSM algorithm, highlighting its significant potential for practical applications in CB-XLCT reconstruction.

#### 4.1.2. Dual-source experiment

The reconstruction results of the dual-light experiment are illustrated in Fig. 4. Quantitative assessments of the five techniques are also summarized in Table 3.

As shown in Fig. 4, the reconstruction performance of the VB-LSM technique is consistently shown to surpass that of the other four methods. The quantitative results presented in Table 3 further substantiate this conclusion. LE of 0.243 mm and 0.378 mm was obtained with the VB-LSM method, indicating that the reconstructed light-source positions were closer to the true

Optics EXPRESS

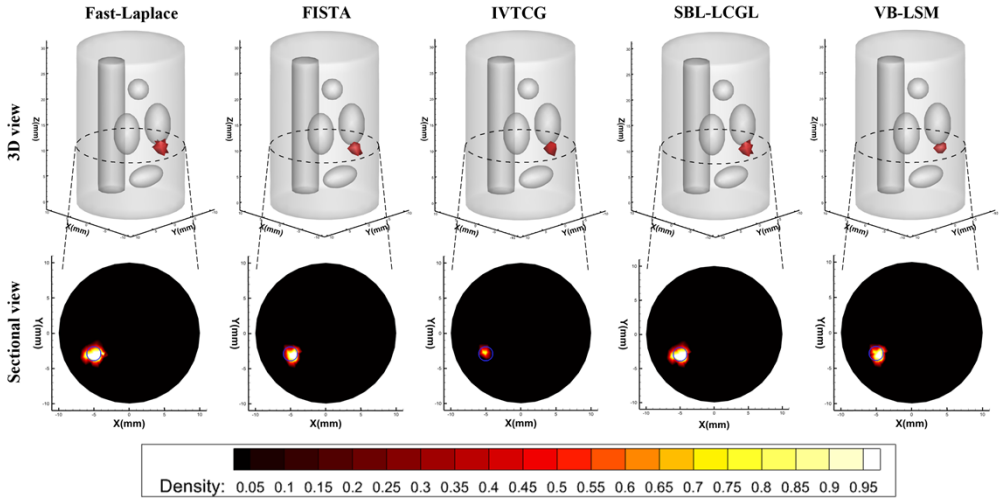


**Fig. 3.** Reconstruction results of five methods for the single-source experiment. The first row shows the 3D views of the four methods, with the red regions representing the reconstructed light sources. The second row presents the reconstructed sectional views on the $Z = 11$ mm plane, where the red-to-yellow regions indicate the reconstructed profile, and the blue circles represent the true target positions and their corresponding boundaries.

**Table 2. Quantitative analysis results of the single-source simulation experiment**

| Method | Target source (mm) | Reconstructed source (mm) | LE (mm) | DICE | Time (s) |
|---|---|---|---|---|---|
| Fast-Laplace | (-5, -3, 11) | (-4.614, -3.182, 10.729) | 0.803 | 0.332 | 54.381 |
| FISTA | (-5, -3, 11) | (-4.687, -3.197, 11.271) | 0.620 | 0.444 | 61.356 |
| IVTCG | (-5, -3, 11) | (-4.525, -2.895, 11.232) | 0.539 | 0.615 | 47.068 |
| SBL-LCGL | (-5, -3, 11) | (-4.767, -3.241, 11.218) | 0.577 | 0.500 | 52.166 |
| VB-LSM | (-5, -3, 11) | (-4.735, -3.101, 10.947) | 0.277 | 0.857 | 48.327 |

Optics EXPRESS

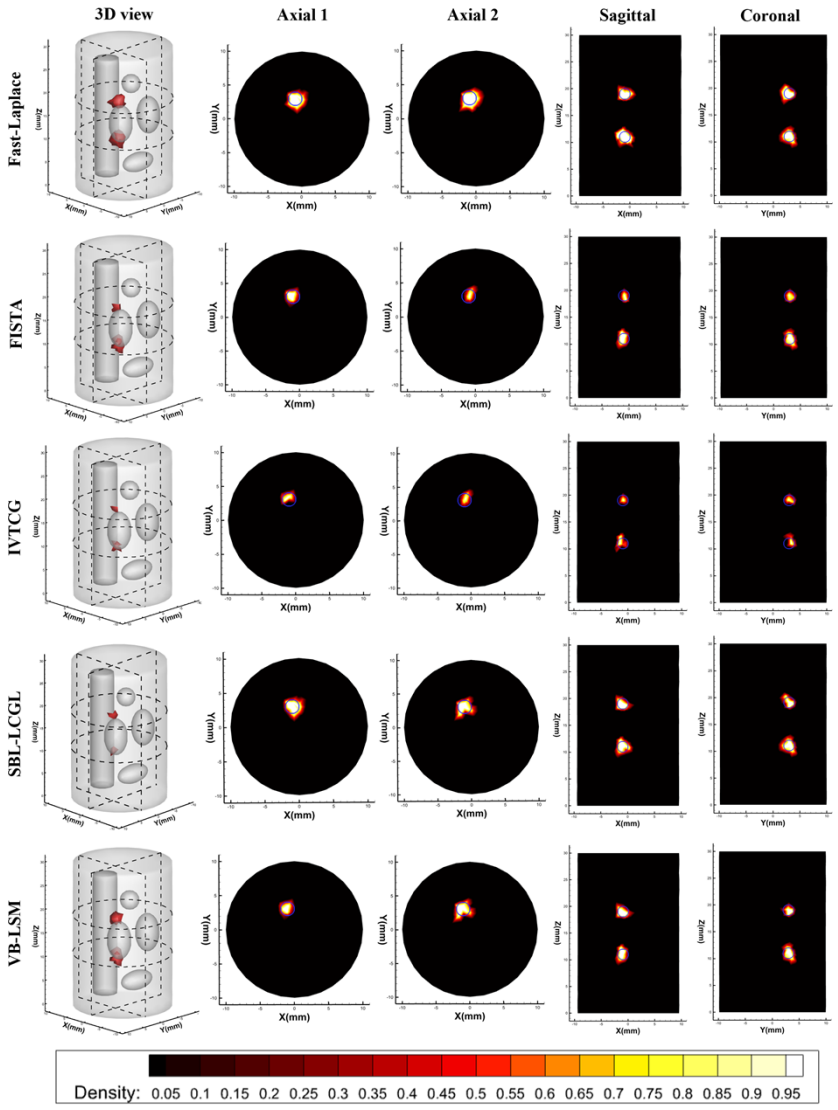


**Fig. 4.** Reconstruction results of five methods for the dual-source experiment. The first column presents the 3D view produced by four distinct methods, with the red regions representing the reconstructed light sources. The second to fifth columns present the axial view (two slices), sagittal view, and coronal view for each method, where the red-to-yellow regions indicate the reconstructed profile, and the blue circles represent the true target positions and their corresponding boundaries.

sources. The mean DICE reached 0.820, demonstrating considerable spatial overlap with the actual emission region, while the computational time was measured at 91.937 s, slightly exceeding the average. In summary, the VB-LSM algorithm markedly reduces positional inaccuracies and improves the precision of source localization and reconstruction under multi-source conditions.

#### 4.1.3. Anti-noise experiment

As shown in Fig. 5, the results of the noise-resilience experiment indicate that, as the proportion of Gaussian noise was progressively increased, the reconstruction performance of the VB-LSM

Optics EXPRESS

**Table 3. Quantitative analysis results of the dual-source simulation experiment**

| Method | Target source (mm) | Reconstructed source (mm) | LE (mm) | Total LE (mm) | DICE | Time (s) |
|---|---|---|---|---|---|---|
| Fast-Laplace | (-1, 3, 11) | (-1.329, 3.193, 11.240) | 0.851 | 0.844 | 0.160 | 103.851 |
| | (-1, 3, 19) | (-1.348, 3.154, 19.207) | 0.836 | | 0.178 | |
| FISTA | (-1, 3, 11) | (-1.241, 3.162, 11.197) | 0.775 | 0.739 | 0.231 | 126.020 |
| | (-1, 3, 19) | (-1.034, 3.316, 18.639) | 0.702 | | 0.334 | |
| IVTCG | (-1, 3, 11) | (-1.493, 3.348, 11.223) | 0.670 | 0.635 | 0.381 | 85.094 |
| | (-1, 3, 19) | (-1.064, 3.457, 18.941) | 0.600 | | 0.471 | |
| SBL-LCGL | (-1, 3, 11) | (-1.371, 3.108, 11.189) | 0.448 | 0.420 | 0.796 | 86.340 |
| | (-1, 3, 19) | (-1.135, 3.265, 18.889) | 0.392 | | 0.642 | |
| VB-LSM | (-1, 3, 11) | (-1.120, 2.899, 11.080) | 0.243 | 0.311 | 0.889 | 91.937 |
| | (-1, 3, 19) | (-0.861, 3.129, 18.923) | 0.378 | | 0.750 | |

method was maintained at a relatively stable level. The LE was observed to rise from 0.2 mm to 0.26 mm, representing a modest increment, while the DICE was reduced from 0.92 to 0.81, corresponding to a decline in spatial overlap of only 11.96%. These results demonstrate that high reconstruction accuracy can be preserved under noisy conditions, reflecting substantial noise resilience and robustness. Even under 25% noise contamination, the VB-LSM approach was able to effectively recover both the spatial structure and intensity characteristics of the light source, further confirming its strong adaptability for practical applications.

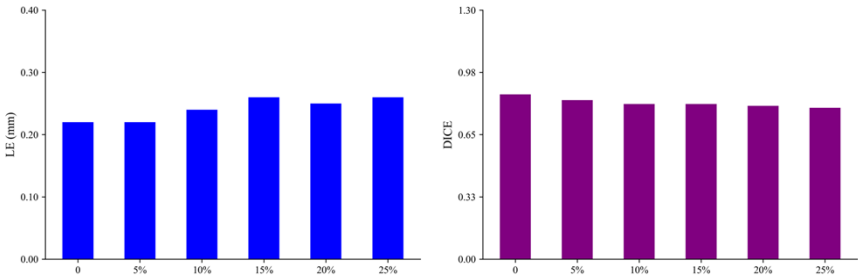


**Fig. 5.** Anti-noise experiment results.

### *4.2. Implantation experiment*

The reconstruction results of the implantation experiment are depicted in Fig. 6. Furthermore, quantitative metrics were calculated and summarized in Table 4. As shown in Fig. 6, the results produced by the Fast-Laplace and SBL-LCGL methods were found to be excessively dispersed, whereas those obtained with FISTA and IVTCG were observed to be overly concentrated. In contrast, artifacts were effectively mitigated by the VB-LSM approach during the reconstruction process, resulting in a clearer depiction of the light-source distribution. The LE between the

Optics EXPRESS

reconstructed and actual light sources was determined to be 0.237 mm, and the DICE was recorded as 0.860. Furthermore, the computational time was comparatively low, indicating that the VB-LSM method can efficiently capture the spatial arrangement of the light source while preserving high morphological fidelity. In summary, VB-LSM demonstrates marked advantages in spatial localization, morphological restoration, and parameter retrieval, thus providing a solid foundation for high-precision CB-XLCT reconstruction.

## 5. Discussion and conclusion

Cone-beam X-ray luminescence computed tomography (CB-XLCT) is a hybrid imaging modality

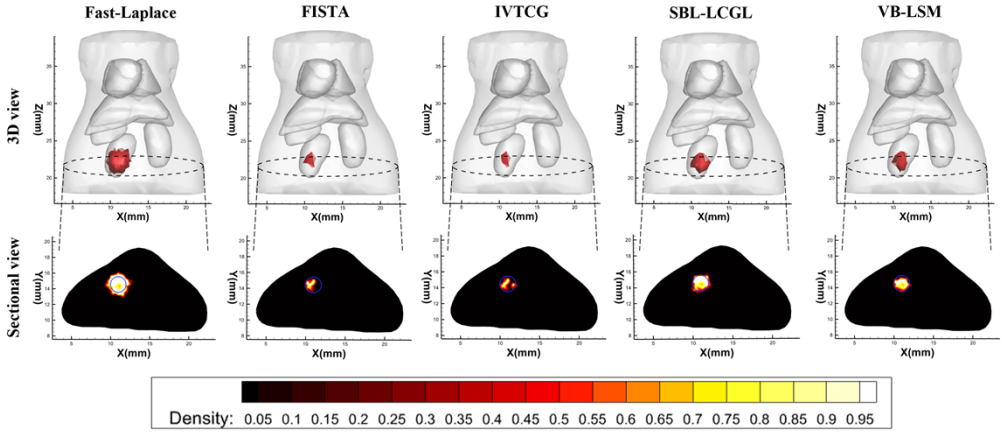


**Fig. 6.** Reconstruction results of the implantation experiment. The first row shows the 3D views of the five methods, with the red regions representing the reconstructed light sources. The second row presents the reconstructed sectional views on the $Z = 21$ mm plane, where the red-to-yellow regions indicate the reconstructed profile, and the blue circles represent the true target positions and their corresponding boundaries.

**Table 4. Quantitative analysis results of the implantation experiment**

| Method | Target source (mm) | Reconstructed source (mm) | LE (mm) | DICE | Time (s) |
|---|---|---|---|---|---|
| Fast-Laplace | (11, 14.5, 21) | (10.742, 14.804, 20.751) | 0.892 | 0.319 | 213.529 |
| FISTA | (11, 14.5, 21) | (10.679, 14.699, 21.045) | 0.637 | 0.484 | 197.318 |
| IVTCG | (11, 14.5, 21) | (10.798, 14.845, 20.814) | 0.589 | 0.693 | 155.766 |
| SBL-LCGL | (11, 14.5, 21) | (10.968, 14.874, 20.871) | 0.503 | 0.772 | 152.694 |
| VB-LSM | (11, 14.5, 21) | (10.872, 14.720, 20.843) | 0.237 | 0.860 | 159.381 |

that enables the reconstruction of the three-dimensional distribution of targeted probes within biological tissues. Nonetheless, its widespread application in biomedical fields has been constrained due to suboptimal reconstruction quality arising from ill-conditioning. In this study, the VB-LSM approach was proposed to enhance the reconstruction performance of CB-XLCT. The employed method utilizes an LSM prior to modeling sparse signals, thereby augmenting the sparsity representation of the excitation source. To realize sparse Bayesian inference based

Optics EXPRESS

on the LSM prior, multiple optimization strategies have been incorporated into the VB-LSM method. Firstly, the scale parameter of the Laplace distribution is assumed to follow an inverse Gamma distribution, facilitating conjugate inference with the Laplace prior and thereby reducing computational complexity. Secondly, the Laplace approximation is applied to approximate the posterior distribution of the sparse signal as a Gaussian distribution, with the expectation demonstrated to correspond to the MAP estimate. Finally, a variational Bayesian inference procedure has been derived based on the EM algorithm, enabling the efficient recovery of sparse signals. The characteristics of sparse signals have thus been accurately captured by the proposed method, resulting in improved reconstruction accuracy and demonstrating particular suitability for CB-XLCT imaging tasks.

To evaluate the performance of the VB-LSM method, numerical simulations and implantation experiments were conducted. The Fast-Laplace, FISTA, IVTCG and SBL-LCGL methods were used for qualitative and quantitative comparisons. In the numerical simulations, single-source, dual-source, and anti-noise experiments were designed. The results consistently indicated that the LE of the VB-LSM method remained below 0.4 mm, while the DICE exceeded 0.7. The stability of both metrics was maintained under varying noise conditions (5%, 10%, 15%, 20%, 25%), demonstrating that the VB-LSM approach possesses not only strong robustness but also high precision in localization and source reconstruction. In the implantation experiment, a flexible plastic sphere containing nanophosphors was implanted into a mouse in order to assess practical performance in tumor localization and morphological reconstruction. Consistent with numerical simulation experiments, our proposed VB-LSM method achieves the lowest LE of 0.237 mm and the highest DICE of 0.860, yielding superior localization and morphological reconstruction results. These findings further underscore the considerable potential of the VB-LSM method for biomedical imaging applications.

Although the VB-LSM method has exhibited superior performance in CB-XLCT reconstruction compared with existing approaches, several critical challenges have yet to be addressed. First, the incorporation of flexible priors has been shown to enhance reconstruction quality; however, the approximation error introduced by the Laplace approximation has not been fully eliminated. Second, validation has primarily been restricted to implanted models and has not encompassed more complex animal experimental conditions. In future work, experiments will be conducted in tumor-bearing mouse models, which more closely replicate physiological conditions, to assess the feasibility and robustness of this approach in practical applications. On this basis, further investigations will be directed toward the development of advanced inference strategies to mitigate the aforementioned approximation error, and a systematic evaluation of VB-LSM will be performed across other optical tomography modalities, including Cerenkov luminescence tomography (CLT), bioluminescence tomography (BLT), and fluorescence molecular tomography (FMT), to assess its potential utility in diverse imaging scenarios.

In summary, the proposed VB-LSM approach achieves high-precision morphological CB-XLCT reconstruction of tumor regions. Sparse signals are modeled using an LSM prior within the VB-LSM technique, thereby enhancing the capability for sparse representation. Through the integration of variational inference, Laplace approximation, and the EM algorithm, accurate reconstruction of sparse signals is enabled. The method has been validated by numerical simulations and implantation experiments. The reconstruction findings indicate that compared to alternative approaches, superior performance in localization accuracy, morphological restoration, and noise robustness is exhibited by the proposed strategy. Future investigations will focus on developing more advanced estimation techniques and promoting the application of this method in both preclinical and clinical settings.

**Funding.** National Major Scientific Research Instrument Development Projects of China (82127805); Key Research and Development Program of Shaanxi Province (2024SF-YBXM-681); National Natural Science Foundation of China (61701403, 61806164).

Optics EXPRESS

**Disclosures.** The authors declare no conflicts of interest.

**Data availability.** Data underlying the results presented in this paper are not publicly available at this time but may be obtained from the authors upon request.

## References


1. G. Pratx, C. M. Carpenter, C. Sun, *et al.*, "X-ray luminescence computed tomography via selective excitation: a feasibility study," IEEE Trans. Med. Imaging **29**(12), 1992–1999 (2010).
2. M. Koch, P. Symvoulidis, and V. Ntziachristos, "Tackling standardization in fluorescence molecular imaging," Nat. Photonics **12**(9), 505–515 (2018).
3. H. Guo, J. Yu, Z. Hu, *et al.*, "A hybrid clustering algorithm for multiple-source resolving in bioluminescence tomography," J. Biophotonics **11**(4), e201700056 (2018).
4. C. Qin, J. Zhong, Z. Hu, *et al.*, "Recent advances in Cerenkov luminescence and tomography imaging," IEEE J. Select. Topics Quantum Electron. **18**(3), 1084–1093 (2012).
5. C. Li, K. Di, J. Bec, *et al.*, "X-ray luminescence optical tomography imaging: experimental studies," Opt. Lett. **38**(13), 2339–2341 (2013).
6. G. Pratx, C. M. Carpenter, C. Sun, *et al.*, "Tomographic molecular imaging of x-ray-excitable nanoparticles," Opt. Lett. **35**(20), 3345–3347 (2010).
7. X. Liu, Q. Liao, and H. Wang, "Fast x-ray luminescence computed tomography imaging," IEEE Trans. Biomed. Eng **61**(6), 1621–1627 (2013).
8. H. Pu, P. Gao, J. Rong, *et al.*, "Spectral-resolved cone-beam X-ray luminescence computed tomography with principle component analysis," Biomed. Opt. Express **9**(6), 2844–2858 (2018).
9. Z. Hu, X. Chen, J. Liang, *et al.*, "Single photon emission computed tomography-guided Cerenkov luminescence tomography," J. Appl. Phys. (Melville, NY, U. S.) **112**(2), 024703 (2012).
10. P. Zhang, C. Ma, F. Song, *et al.*, "A review of advances in imaging methodology in fluorescence molecular tomography," Phys. Med. Biol. **67**(10), 10TR01 (2022).
11. D. Chen, S. Zhu, X. Chen, *et al.*, "Quantitative cone beam X-ray luminescence tomography/X-ray computed tomography imaging," Appl. Phys. Lett. **105**(19), 191104 (2014).
12. D. Chen, S. Zhu, H. Yi, *et al.*, "Cone beam x-ray luminescence computed tomography: A feasibility study," Med. Phys **40**(3), 031111 (2013).
13. X. He, X. Wang, H. Yi, *et al.*, "Laplacian manifold regularization method for fluorescence molecular tomography," J. Biomed. Opt **22**(4), 045009 (2017).
14. J. Zhao, H. Guo, J. Yu, *et al.*, "A robust elastic net-$\ell$ 1 $\ell$ 2 reconstruction method for x-ray luminescence computed tomography," Phys. Med. Biol. **66**(19), 195005 (2021).
15. H. Zhang, G. Geng, S. Zhang, *et al.*, "Sparse non-convex lp regularization for cone-beam x-ray luminescence computed tomography," J. Mod. Opt. **65**(20), 2278–2289 (2018).
16. P. Gao, K. Cheng, E. Schüler, *et al.*, "Restarted primal–dual Newton conjugate gradient method for enhanced spatial resolution of reconstructed cone-beam x-ray luminescence computed tomography images," Phys. Med. Biol. **65**(13), 135008 (2020).
17. X. Liu, S. Ma, S. Zhong, *et al.*, "Permissible region extraction strategies for XLCT: a comparative study," J. Phys.: Conf. Ser. **2112**(1), 012001 (2021).
18. T. Liu, J. Ruan, J. Rong, *et al.*, "Cone-beam X-ray luminescence computed tomography based on MLEM with adaptive FISTA initial image," Computer Methods and Programs in Biomedicine **229**, 107265 (2023).
19. S. Singh and R. S. Anand, "Multimodal medical image sensor fusion model using sparse K-SVD dictionary learning in nonsubsampled shearlet domain," IEEE Trans. Instrum. Meas. **69**(2), 593–607 (2020).
20. Y. Chen, M. Du, G. Zhang, *et al.*, "Sparse reconstruction based on dictionary learning and group structure strategy for cone-beam X-ray luminescence computed tomography," Opt. Express **31**(15), 24845–24861 (2023).
21. W. Li, W. Lu, X. Liang, *et al.*, "Collaborative Dictionary Learning for Compressed Sensing," IEEE Trans. Ind. Inf. **20**(7), 9610–9620 (2024).
22. G. Zhang, F. Liu, J. Liu, *et al.*, "Cone beam x-ray luminescence computed tomography based on Bayesian method," IEEE Trans. Med. Imaging **36**(1), 225–235 (2017).
23. W. Cheng, L. Ma, T. Yang, *et al.*, "Joint lung CT image segmentation: A hierarchical Bayesian approach," PLoS One **11**(9), e0162211 (2016).
24. X. Li, C. X. Ling, and H. Wang, "The convergence behavior of naive Bayes on large sparse datasets," ACM Trans. Knowl. Discov. Data **11**(1), 1–24 (2017).
25. Y. Wang, H. Wang, Q. Zhu, *et al.*, "SBL-LCGL: sparse Bayesian learning based on Laplace distribution for robust cone-beam x-ray luminescence computed tomography," Phys. Med. Biol. **69**(17), 175020 (2024).
26. Y. Sun, L. Zhang, T. Fei, *et al.*, "Variational Bayesian blind restoration reconstruction based on shear wave transform for low-dose medical CT image," J Image Video Proc. **2017**(1), 84 (2017).
27. H. Mkindu, L. Wu, and Y. Zhao, "Lung nodule detection in chest CT images based on vision transformer network with Bayesian optimization," Biomed. Signal Process. Control **85**, 104866 (2023).
28. I. Seferis, C. Michail, I. Valais, *et al.*, "Imaging performance of a thin Lu2O3: Eu nanophosphor scintillating screen coupled to a high resolution CMOS sensor under X-ray radiographic conditions: comparison with Gd2O2S: Eu conventional phosphor screen," Med. Imaging 2014: Phys. Med. Imaging **9033**, 1095–1100 (2014).

Optics EXPRESS

29. A. D. Klose, V. Ntziachristos, and A. H. Hielscher, "The inverse source problem based on the radiative transfer equation in optical molecular imaging," J. Comput. Phys. **202**(1), 323–345 (2005).
30. Z. Hu, M. Zhao, Y. Qu, *et al.*, "In vivo 3-dimensional radiopharmaceutical-excited fluorescence tomography," J. Nucl. Med **58**(1), 169–174 (2017).
31. C. M. Bishop and M. Tipping, "Variational relevance vector machines," arXiv (2013).
32. M. E. Tipping, "Sparse Bayesian learning and the relevance vector machine," J. Mach. Learn. Res **1**, 211–244 (2001).
33. G. Tzagkarakis, D. Milioris, and P. Tsakalides, "Multiple-measurement Bayesian compressed sensing using GSM priors for DOA estimation," in *ICASSP*, 2610–2613 (IEEE, 2010).
34. J. Zhao, X. Bai, T. Shan, *et al.*, "Block sparse Bayesian recovery with correlated LSM prior," Wirel. Commun. Mob. Comput **2021**(1), 9942694 (2021).
35. E. Levitan and G. T. Herman, "A maximum a posteriori probability expectation maximization algorithm for image reconstruction in emission tomography," IEEE Trans. Med. Imaging **6**(3), 185–192 (1987).
36. C. Wang and D. M. Blei, "Variational inference in nonconjugate models," J. Mach. Learn. Res **14**(1), 1005–1031 (2013).
37. G. Zhang, J. Zhang, Y. Chen, *et al.*, "Logarithmic total variation regularization via preconditioned conjugate gradient method for sparse reconstruction of bioluminescence tomography," Computer Methods and Programs in Biomedicine **243**, 107863 (2024).
38. Y. Chen, M. Du, J. Zhang, *et al.*, "Generalized conditional gradient method with adaptive regularization parameters for fluorescence molecular tomography," Opt. Express **31**(11), 18128–18146 (2023).
39. N. Ren, J. Liang, X. Qu, *et al.*, "GPU-based Monte Carlo simulation for light propagation in complex heterogeneous tissues," Opt. Express **18**(7), 6811–6823 (2010).